ARTICLE

Electronically Modulated FeNi Composite by CeO_2 Porous Nanosheets for Water Splitting at Large Current Density

Ming-Yu Ding, Wen-Jie Jiang, Tian-Qi Yu, Xiao-Yan Zhuo, Xiao-Jing Qin, Shi-Bin Yin*

Guangxi Key Laboratory of Electrochemical Energy Materials, School of Chemistry and Chemical Engineering, Guangxi University, Guangxi Nanning, 530004, China

Abstract

Exploiting highly active and non-noble metal bifunctional catalysts at large current density is significant for the advancement of water electrolysis. In this work, CeO_2 electronically structure modulated FeNi bimetallic composite porous nanosheets *in-situ* grown on nickel foam ($NiFe_2O_4$-$Fe_{24}N_{10}$-CeO_2/NF) is synthesized. Electrochemical experiments show that the $NiFe_2O_4$-$Fe_{24}N_{10}$-CeO_2/NF exhibited the outstanding activities toward both oxygen and hydrogen evolution reactions (OER and HER) ($\eta_{1000} = 352$ mV and $\eta_{1000} = 429$ mV, respectively). When assembled into a two-electrode system for overall water splitting (OWS), it only needs a low cell voltage of 1.81 V to drive 100 $mA \cdot cm^{-2}$. And it can operate stably at ± 500 $mA \cdot cm^{-2}$ over 30 h toward OER, HER and OWS without significant activity changes. The reason could be assigned to the electronic modulating of CeO_2 on FeNi composite, which can boost the intrinsic activity and optimize the adsorption of reaction intermediates. Moreover, the porous nanosheets *in-situ* grown on NF could enhance the contact of active site with electrolyte and facilitate the gas release, thus improving its chemical and mechanical stabilities. This study highlights a novel approach to design bifunctional non-noble metal catalysts for water splitting at large current density.

Keywords: FeNi composite; Hydrogen evolution reaction; Oxygen evolution reaction; Catalyst; Water splitting

1. Introduction

The development of hydrogen energy with zero pollution and high combustion calorific value will enable the transition from traditional energy to clean and sustainable hydrogen economy [1−3]. Water electrolysis driven by renewable energy (e.g., wind and solar) to produce H_2 is deemed a promising method. However, its practical application is hindered due to the slow reaction kinetics and high overpotential [4,5]. Although the above issues have been deeply studied, it is still difficult to meet the requirements of long-term and efficient operation at large current densities in industrial water electrolysis for hydrogen production [6]. It is still challenging to design catalysts with abundant active sites and good durability/efficiency at large current density.

Among various catalysts, Fe-Ni-based composites have been considered as ideal catalysts for OER because of their high intrinsic activity and fast kinetics under alkaline conditions [7−9]. And there exists synergistic effect between Ni and Fe compared with single-component catalysts, which can effectively improve the intrinsic activity [10−12]. Meanwhile, Fe-Ni-based composites could form the FeNi double metal oxyhydroxide (NiFeOOH) during OER, thus Fe^{3+} occupies an octahedral position in NiFeOOH, and the Fe-O bond length is very short due to the influence of the surrounding edge-sharing octahedron (NiO_6) [13]. This structure can facilitate the adsorption of oxygen-containing intermediates during OER, therefore enhancing the reaction rate [14]. Nevertheless, most Fe-Ni-based composite materials are only used for OER because of the weak bonding

Received 12 August 2022; Received in revised form 19 September 2022; Accepted 14 November 2022
Available online 21 November 2022

* Corresponding author, Shi-Bin Yin, Tel: (86-771)3233718, E-mail address: yinshibin@gxu.edu.cn.

https://doi.org/10.13208/j.electrochem.2208121

between hydrogen and Fe^{3+} [15,16]. Thereby designing advanced multifunctional catalysts is necessary.

According to previous studies, combination of CeO_2 with transition metals could enhance the intrinsic HER activity [17,18]. CeO_2 as a water dissociation promoter exhibits excellent electronic/ionic conductivity due to the abundant half-filled and empty *d* orbitals, thereby lowering the energy barrier for the formation of hydrogen intermediates [19,20]. Chen et al. prepared a composite with CeO_2 modulating the electronic structure of Ni that is favorable for the transportations of electrons and ions to exhibit good HER activity [21]. Besides, CeO_2 is usually applied as OER catalysts because of its superior conductivity and oxygen storage ability accompanied by reversible exchange states between Ce^{3+} and Ce^{4+} [22,23]. Li and co-workers synthesized a FeOOH/CeO_2 hetero-layered nanotube, which exhibited better OER performance than single FeOOH component [24].

The long-term stable operation of catalysts at large current density is another key factor for realizing industrial applications, since the vigorous reactions of anode and cathode will cause catalyst shedding and structural damage [25,26]. Morphology control and substrate selection are considered as efficient methods to enhance catalyst stability [27,28]. Among them, two-dimensional (2D) nanosheet *in-situ* grown on conductive substrate (NF) has the advantages of the stable combination between the active species and substrate, which is beneficial for accelerating electron and ion transfers [29,30]. As well as possessing large specific area to facilitate gas release, thus avoiding catalyst shedding and structural damage [31]. In our previous work [32], IrNi-$FeNi_3$ hybrid nanosheets are synthesized on NF *via* one-step solvothermal, which could maintain at 1000 $mA \cdot cm^{-2}$ for 100 h in industrial conditions.

Herein, $NiFe_2O_4$-$Fe_{24}N_{10}$-CeO_2 composite with porous nanosheets structure *in-situ* grown on NF ($NiFe_2O_4$-$Fe_{24}N_{10}$-CeO_2/NF) is designed and prepared by solvothermal and annealing treatments (Fig. 1). It combines the advantages of CeO_2 in regulating electronic structure and self-supporting porous nanosheets, showing the feasibility of high-efficiency, stable and low-cost water electrolysis at large current density. The electrochemical characterization demonstrates that it arrived at ± 1000 $mA \cdot cm^{-2}$ only requiring overpotentials of 352 and 429 mV for OER and HER, respectively. Moreover, when used as a two-electrode system for water electrolysis, it needs a low voltage of 1.81 V to reach 100 $mA \cdot cm^{-2}$, which surpasses those of $NiFe_2O_4$-$Fe_{24}N_{10}$/NF (1.83 V), CeO_2/NF (1.94 V) and precursor (1.89 V), and it could also operate stably at 500 $mA \cdot cm^{-2}$ for 30 h.

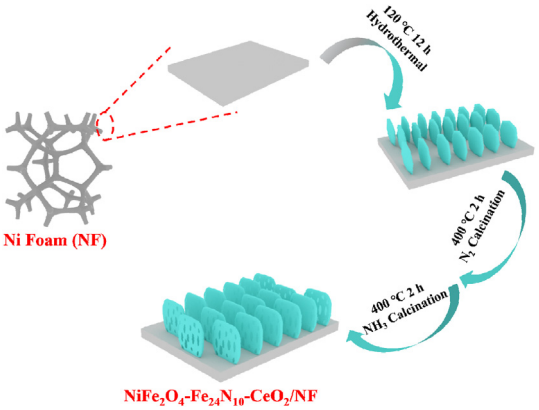

Fig. 1. Schematic diagram for the synthesis of $NiFe_2O_4$-$Fe_{24}N_{10}$-CeO_2/NF.

2. Experimental section

2.1. Materials

All reagents were of analytical grade and used directly without further purification, including ferric nitrate nonahydrate ($Fe(NO_3)_3 \cdot 9H_2O$), nickel foam (NF), urea (H_2NCONH_2), cerium nitrate hexahydrate ($Ce(NO_3)_3 \cdot 6H_2O$), potassium hydroxide (KOH), hydrochloric acid (HCl) and absolute ethanol (C_2H_5OH).

2.2. Syntheses of $NiFe_2O_4$-$Fe_{24}N_{10}$-CeO_2/NF, $NiFe_2O_4$-$Fe_{24}N_{10}$/NF and CeO_2/NF

NF (1.0 cm × 6.0 cm) was sonicated with 1.0 $mol \cdot L^{-1}$ HCl solution to reduce the influence of oxide layer on the reaction, followed by repeated cleaning with absolute ethanol and DI water for several times, respectively. $Fe(NO_3)_3 \cdot 9H_2O$ (252.75 mg), $Ce(NO_3)_3 \cdot 6H_2O$ (271.5 mg) and H_2NCONH_2 (363.75 mg) were added into 30 mL DI water, then the solution and pretreated NF were transferred into 50 mL Teflon-lined autoclave for 12 h heating treatment at 120 °C. Subsequently, the obtained precursors were annealed at 400 °C for 2 h under nitrogen (N_2) environment and then bubbled with ammonia (NH_3) for additional 2 h $NiFe_2O_4$-$Fe_{24}N_{10}$/NF and CeO_2/NF were also prepared by the similar procedure without Ce and Fe sources, respectively. To load the commercial Pt/C or 40 wt% IrO_2/C catalyst on Ni foam, 5.0 mg of catalyst powders were dispersed in 1.0 mL (20.0 μL 5.0 wt% Nafion and 0.98 mL ethanol) solution. The suspension was sonicated for 30 min to prepare a homogeneous ink. The NF with a fixed area was drop-casted with 40 μL of the catalyst ink.

2.3. Material characterizations

The morphology of the above samples was investigated using scanning electron microscope (SEM, SU8220, Hitachi Corp.). Transmission electron microscopic (TEM) and elemental distribution observations were performed on Titan ETEM (TALOS 200X, FEI Corp.). X-ray diffraction (XRD, Rigaku Corp., with a copper *K*-edge X-ray) was utilized to determine the structure of the specimens. X-ray photoelectron spectroscopic (XPS) measurement was performed on an instrument (ESCALAB-250Xi, Thermo Fisher) with a monochromatic Al (300 W) K_α X-ray line source.

2.4. Electrochemical measurements

Electrochemical test was performed in a three-electrode system (Interface 1010E, Gamry, USA) at 30 °C in N_2 saturated 1.0 mol·L^{-1} KOH solution. Hg/HgO electrode and graphite rod were used as the reference and counter electrode, respectively. All potentials were calibrated against the reversible hydrogen electrode (RHE) according to Nernst equation ($E_{RHE} = E_{Hg/HgO} + 0.0591 \times pH + 0.098$). Cyclic Voltammetric (CV) activation at a scan rate of 100 mV·s^{-1} was performed for 10 cycles prior to conduct the linear sweep voltammetric (LSV) test at a scan rate of 5 mV·s^{-1} for characterizing the OER, HER and OWS activities of each sample. Unless otherwise specified, all the polarization curves were *iR*-corrected, where i is the experimentally measured current and R is the solution resistance. Electrochemical impedance spectroscopic (EIS) measurements were performed in the frequency range from 100 kHz to 0.1 Hz, and the polarization voltages were −0.20 V (HER) and 1.55 V (OER). The Tafel plots were obtained *via* Tafel equation: $\eta = a + b\log|j|$, where a, b and j are intercept, Tafel slop and current density, respectively.

3. Results and discussion

The microscopic morphologies of precursor and $NiFe_2O_4$-$Fe_{24}N_{10}$-CeO_2/NF were observed by SEM. The nanosheets structures of precursor are smooth and vertically distributed on NF (Fig. S1a, b). The $NiFe_2O_4$-$Fe_{24}N_{10}$-CeO_2/NF with rough and porous structure is formed after annealing at 400 °C in NH_3 atmosphere (Fig. S1c, d), which could increase the active specific surface area of the catalyst to expose abundant active sites [33]. Meanwhile, this structure facilitates the contact between electrolyte and active sites, as well as bubbles escape, thereby improving the catalytic efficiency. Fig. S2 shows that the morphology of $NiFe_2O_4$-$Fe_{24}N_{10}$/NF consisted of nanosheets and agglomerated nanoparticles, with only a few nanosheets growing on the agglomerated nanoparticles. The reason for this phenomenon could be that $NiFe_2O_4$ is a nanoparticle with uneven size, which is prone to agglomeration, and the introduction of CeO_2 avoids the sintering of $NiFe_2O_4$.

In addition, the $NiFe_2O_4$-$Fe_{24}N_{10}$-CeO_2/NF also shows the nanosheets morphology (Fig. 2a). In Fig. 2b, high-resolution TEM (HRTEM) images demonstrate the lattice distances of 0.251, 0.230 and 0.271 nm, which are derived from $NiFe_2O_4$(311), $Fe_{24}N_{10}$(220) and CeO_2(200) planes, respectively. And Fig. 2c displays the lattice spacings of 0.208, 0.251, 0.230 and 0.271 nm, which could be assigned to $NiFe_2O_4$(400), $NiFe_2O_4$(311), $Fe_{24}N_{10}$(220) and CeO_2(200), respectively. The above crystal planes are also observed in the XRD patterns (Fig. 3a). As shown in Fig. 2d−i, the HAADF-STEM and elemental mappings images demonstrate the homogeneous distributions of Ni, Fe, Ce, O and N on $NiFe_2O_4$-$Fe_{24}N_{10}$-CeO_2/NF nanosheets.

XRD was used to analyze the crystal structure of the prepared powder samples. The peaks located at 30.3°, 35.7°, 57.4° and 63.0° are derived from the (200), (311), (400) and (511) planes of $NiFe_2O_4$ (PDF#74-2081) in Fig. 3a. The reaction process could be as follows: The Fe^{3+} undergoes hydrolysis reaction to generate H^+, and then H^+ and NO_3^- etch the NF to generate Ni^{2+} [34]. Subsequently, H_2O, Ni^{2+} and Fe^{3+} react to form $NiFe_2O_4$ *in-situ* on the surface of NF. The characteristic peaks at 39.1° (201), 41.5° (002), 44.5° (221) and 58.3° (222) belong to $Fe_{24}N_{10}$ (PDF#73-2103). The diffraction peaks of 28.5°, 33.1°, 47.5° and 56.3° are assigned to the (111), (200), (220) and (311) crystal planes of cubic fluorite CeO_2 (PDF#89-8436). XRD results indicate that the $NiFe_2O_4$-$Fe_{24}N_{10}$-CeO_2 is composed of three phases of $NiFe_2O_4$, $Fe_{24}N_{10}$ and CeO_2. Besides, the XRD patterns of $NiFe_2O_4$-$Fe_{24}N_{10}$/NF and CeO_2/NF are presented in Fig. S3.

Then, to study the discrepancy of surface chemical states and compositions between $NiFe_2O_4$-$Fe_{24}N_{10}$-CeO_2/NF, the XPS data of $NiFe_2O_4$-$Fe_{24}N_{10}$/NF and CeO_2/NF were obtained (Fig. 3b−d). The survey spectrum further proves that $NiFe_2O4$-$Fe_{24}N_{10}$-CeO_2/NF contained Ni, Fe, Ce, N and O elements (Fig. S4a). For fine spectrum of Ni 2p in $NiFe_2O_4$-Fe_24N_{10}-CeO_2/NF (Fig. 3b), the peaks at 855.1 and 872.4 eV can be attributed to Ni^{2+}, and the peaks at 857.0 and 874.3 eV correspond to Ni^{3+}. The high-resolution Fe 2p spectrum consists of Fe^{2+}(710.5/723.6 eV) and Fe^{3+}(713.8/726.9 eV) (Fig. 3c). Significantly, the Ni 2p and Fe 2p of $NiFe_2O_4$-$Fe_{24}N_{10}$-CeO_2/NF display a positive shift (Δ = 0.2 eV) relative to that of $NiFe_2O_4$-

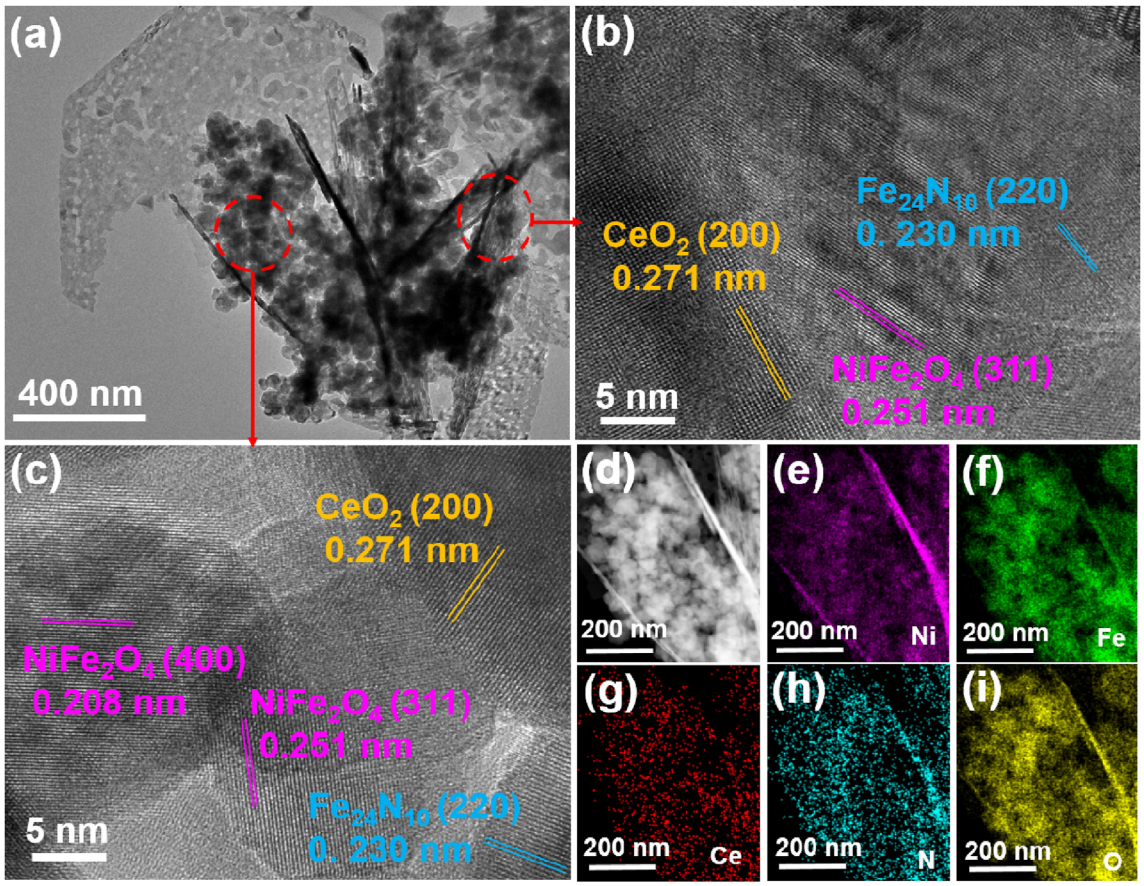

Fig. 2. (a–c) TEM and HRTEM images of $NiFe_2O_4$-$Fe_{24}N_{10}$-CeO_2/NF, (d–i) HAADF-STEM and elemental mappings images.

$Fe_{24}N_{10}$/NF. While the Ce 3d in $NiFe_2O_4$-$Fe_{24}N_{10}$-CeO_2/NF exhibits a distinguished negative binding energy shift (Δ = 0.3 eV) than that of CeO_2/NF (Fig. 3d). These phenomena confirm that CeO_2 acts as an electron acceptor to induce electron transfer from the two-phase $NiFe_2O_4$-$Fe_{24}N_{10}$ to CeO_2 due to the electronic interaction between CeO_2 and $NiFe_2O_4$-$Fe_{24}N_{10}$ [35,36], thereby changing the internal electronic structure [37]. This will optimize the adsorption energy of reaction intermediates, thus improving catalytic performance [38,39]. The N 1s peaks of 397.6 and 399.4 eV correspond to Fe–N and N–H (Fig. S4b). It is reported that Fe–N bonds can reversibly exchange oxygen reaction [40]. The appearance of Fe–N is attributed to the $Fe_{24}N_{10}$ phase, which is generated by the coordination reaction of Fe atoms with N atoms under an ammonia atmosphere. Besides, the O 1s peak is presented in Fig. S4c.

Then electrochemical measurements were performed to assess the activity of catalysts. Fig. 4a displays that $NiFe_2O_4$-$Fe_{24}N_{10}$-CeO_2/NF only requires low overpotential of 274 mV to reach 100 $mA \cdot cm^{-2}$ toward OER, which is better than $NiFe_2O_4$-$Fe_{24}N_{10}$/NF (206 mV), CeO_2/NF (361 mV), NF (342 mV) and IrO_2/C/NF (353 mV). The reason may be that the introduction of CeO_2 can change the electronic structure and enhance the adsorption of intermediates, thereby speeding up the reaction rate. Obviously, the potential of $NiFe_2O_4$-$Fe_{24}N_{10}$-CeO_2/NF relative to precursor (E_{100} = 1.54 V) shifts significantly to a more negative direction, possibly benefitting from the porous structure formed by calcination to expose more active sites. Furthermore, $NiFe_2O_4$-$Fe_{24}N_{10}$-CeO_2/NF still exhibits the best activity among all catalysts, even in harsh environment of large current density with severe reaction, suggesting that it exhibits significant promise for commercial applications. Among them, the activity of IrO_2/C/NF is worse than that of NF due to the introduction of more Nafion binders with non-conductive properties in the preparation of IrO_2/C/NF.

Tafel slopes of $NiFe_2O_4$-$Fe_{24}N_{10}$-CeO_2/NF (62.34 $mV \cdot dec^{-1}$), $NiFe_2O_4$-$Fe_{24}N_{10}$/NF (70.56 $mV \cdot dec^{-1}$), CeO_2/NF (125.47 $mV \cdot dec^{-1}$), IrO_2/C/NF (116.09 $mV \cdot dec^{-1}$), NF (104.49 $mV \cdot dec^{-1}$) and precursor (88.49 $mV \cdot dec^{-1}$) were calculated by polarization curves (Fig. 4b). The minimum Tafel value of $NiFe_2O_4$-$Fe_{24}N_{10}$-CeO_2/NF implies a kinetic advantage relative to other prepared catalysts. It can be interpreted that the micro/nanoarray structure

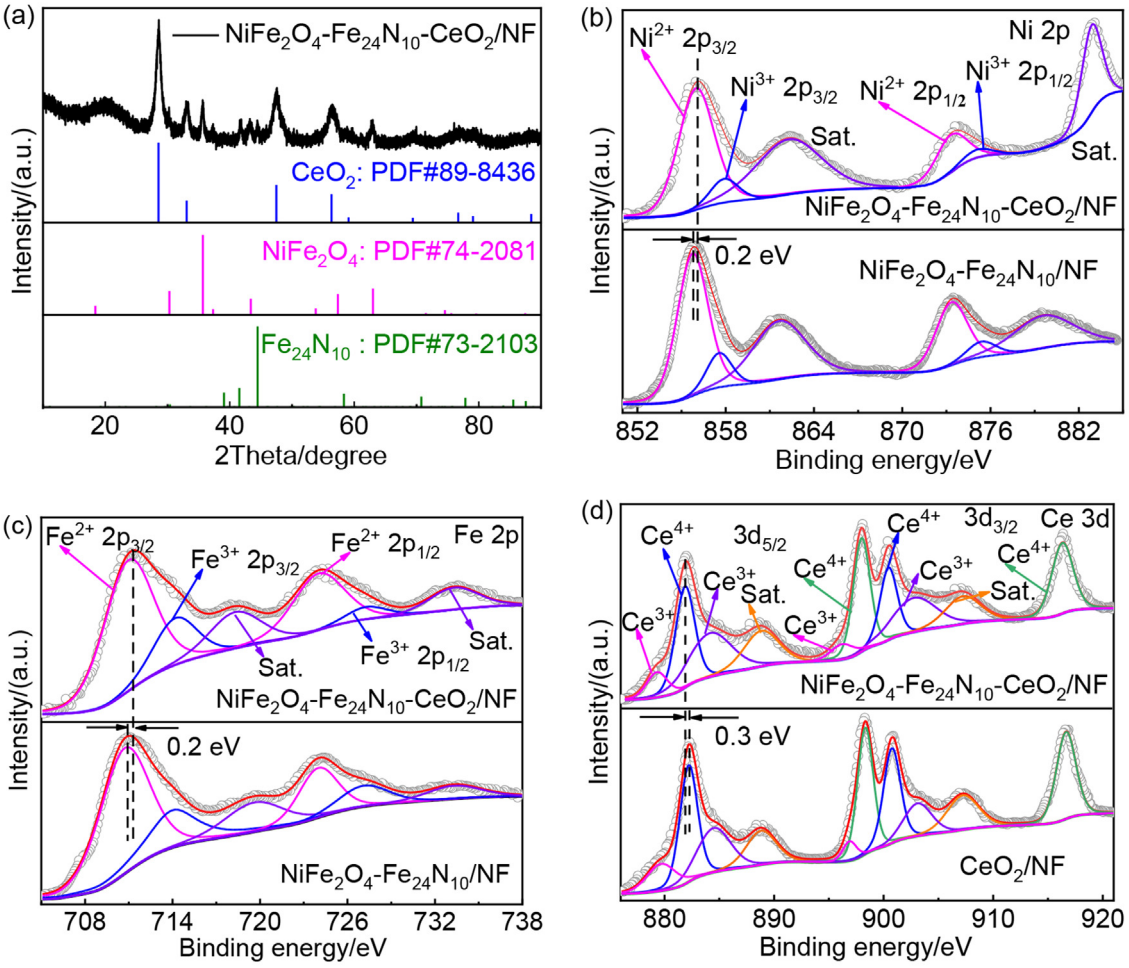

Fig. 3. (a) XRD pattern of $NiFe_2O_4$-$Fe_{24}N_{10}$-CeO_2/NF; XPS spectra of (b) Ni 2p and (c) Fe 2p in $NiFe_2O_4$-$Fe_{24}N_{10}$-CeO_2/NF and $NiFe_2O_4$-$Fe_{24}N_{10}$/NF, and (d) Ce 3d in $NiFe_2O_4$-$Fe_{24}N_{10}$-CeO_2/NF and CeO_2/NF.

formed by the rough nanosheets facilitates the mass transport and exposes abundant active sites, thereby accelerating the reaction kinetics. Besides, according to literatures, $NiFe_2O_4$ is prone to be agglomerated due to its inhomogeneous size of nanoparticles. The introduction of CeO_2 prevents $NiFe_2O_4$ nanoparticles from agglomeration and facilitates the adsorption of water molecules [41]. In Fig. 4b, $NiFe_2O_4$-$Fe_{24}N_{10}$-CeO_2/NF exhibits the smallest charge transfer resistance (R_{ct}) observed by EIS, this is because that the interaction between CeO_2 and $NiFe_2O_4$-$Fe_{24}N_{10}$ accelerates electron transfer.

Chronopotentiometry (CP) method is adopted to evaluate the OER stability of $NiFe_2O_4$-$Fe_{24}N_{10}$-CeO_2/NF (Fig. 4d). It can keep working at 500 $mA \cdot cm^{-2}$ for 30 h (potential change ca. 20 mV), indicating good OER stability. Fig. S5 shows the microstructure changes of catalysts during prolonged O_2 release, the porous nanosheets morphology could be well-remained under harsh conditions. The good OER stability benefits from the porous nanosheets and the regulation of CeO_2, which can alleviate the catalyst agglomerate.

HER activity of $NiFe_2O_4$-$Fe_{24}N_{10}$-CeO_2/NF was also evaluated. Although Pt/C/NF exhibited excellent intrinsic activity with the overpotential of 23 mV at -10 $mA \cdot cm^{-2}$ (Fig. 5a). However, it is fabricated with the assistance of Nafion binder, which cannot operate stably at large current density due to violent bubble release, thus leading to the mechanical shedding of active material. $NiFe_2O_4$-$Fe_{24}N_{10}$-CeO_2/NF only needs an overpotential of 429 mV to stably reach -1000 $mA \cdot cm^{-2}$, which is superior to $NiFe_2O_4$-$Fe_{24}N_{10}$/NF (458 mV), NF (483 mV), precursor (458 mV) and CeO_2/NF. This excellent HER activity could be attributed to the synergy between $NiFe_2O_4$-$Fe_{24}N_{10}$ and CeO_2 optimizes the catalytic activity. As shown in Fig. 5(b and c), except for Pt/C/NF, $NiFe_2O_4$-$Fe_{24}N_{10}$-CeO_2/NF displays smaller Tafel slope and R_{ct} than those of other samples, which implies that the introductions of CeO_2 and

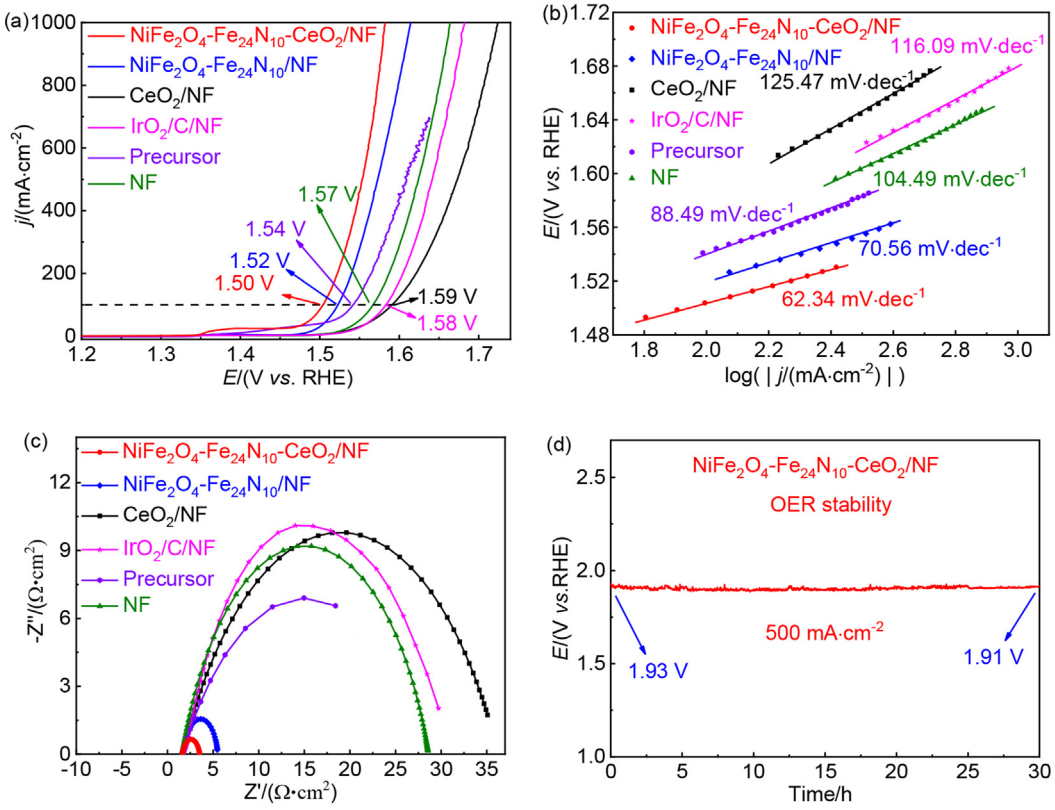

Fig. 4. OER performance tests. (a) LSV curves, (b) Tafel slopes, (c) Nyquist curves, (d) chronopotentiometric curve at 500 mA·cm^{-2}.

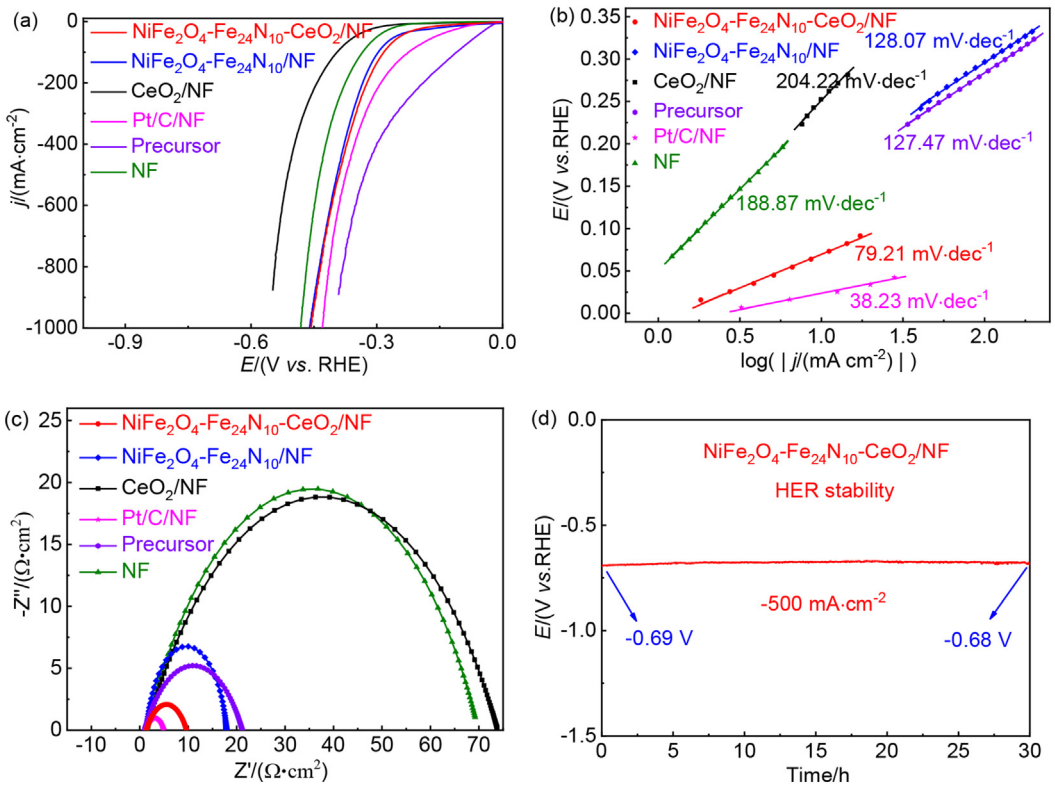

Fig. 5. HER performance tests. (a) LSV curves, (b) Tafel slopes, (c) Nyquist curves, and (d) chronopotentiometric curve at −500 mA·cm^{-2}.

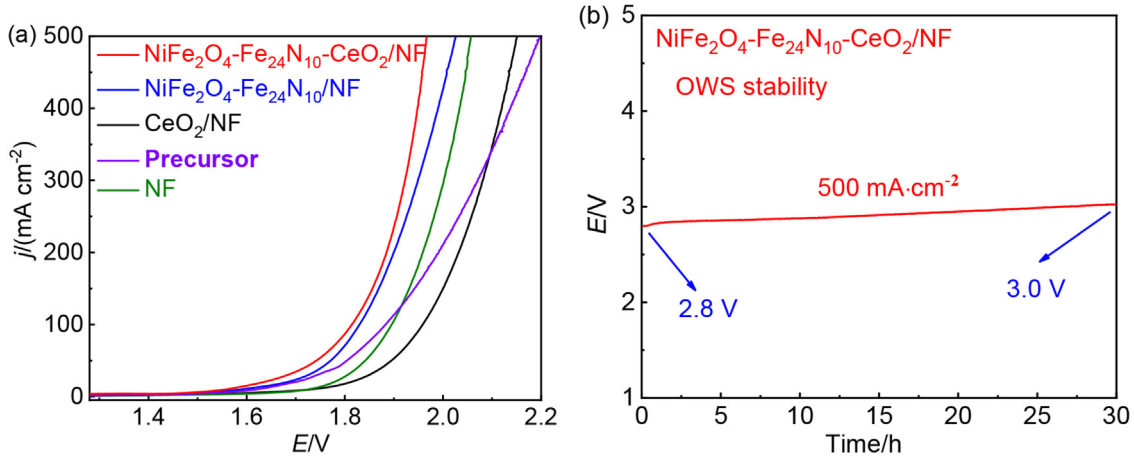

Fig. 6. (a) Overall water splitting LSV curves of $NiFe_2O_4$-$Fe_{24}N_{10}$-CeO_2/NF, $NiFe_2O_4$-$Fe_{24}N_{10}$/NF, CeO_2/NF, precursors and NF; (b) chronopotentiometric curve of $NiFe_2O_4$-$Fe_{24}N_{10}$-CeO_2/NF at 500 mA·cm^{-2}.

porous nanosheets can speed up the electron and mass transfers.

Besides, CP method was also employed to assess the HER stability (Fig. 5d). The potential changed by only 10 mV after $NiFe_2O_4$-$Fe_{24}N_{10}$-CeO_2/NF was continuously operated for 30 h at −500 mA·cm^{-2}, indicating the gratified HER durability. It is also demonstrated by the morphology of $NiFe_2O_4$-$Fe_{24}N_{10}$-CeO_2/NF after long-term H_2 evolution tests, that is, the morphology of porous nanosheets still preserved well (Fig. S6).

Electrochemical surface area (ECSA) is a significant parameter to evaluate the catalysts, which can be calculated by the following formula:

$$\mathrm{ECSA} = C_{\mathrm{dl}}/C_{\mathrm{s}} \quad (1)$$

In Fig. S7, C_{dl} value was estimated by cyclic voltammetry (CV) method in the non-Faraday region (0.8−1.0 V) with the scan rates from 20 to 100 mV·s^{-1}. The $NiFe_2O_4$-$Fe_{24}N_{10}$-CeO_2/NF exhibits the highest C_{dl} value (22.69 mF·cm^{-2}), which is 1.5, 5.9 and 10.8 times higher than those of CeO_2/NF, $NiFe_2O_4$-$Fe_{24}N_{10}$/NF and precursor. The above results clearly demonstrate that the introduction of CeO_2 can increase the ECSA and effective active sites, thereby enhancing the kinetics of the water electrolysis reaction. The reason could be that the presence of CeO_2 avoids the problem of easy agglomeration of $NiFe_2O_4$, thereby exposing active sites. Meanwhile, the porous nanosheet structure of $NiFe_2O_4$-$Fe_{24}N_{10}$-CeO_2/NF after annealing can facilitate the contact between electrolyte and active sites, and thus enriching the activity.

As displayed in Fig. S8, the activity of catalyst was optimized by annealing at different temperatures (300, 400, 500, 600 and 700 °C) under NH_3 atmosphere. The sample prepared at 400 °C has the superior OER and HER activities as well as the fastest kinetics. The annealing temperature will change the chemical composition and microscopic morphology of the catalyst, thereby affecting the catalytic activity.

In Fig. 6a, considering the good HER and OER performances of $NiFe_2O_4$-$Fe_{24}N_{10}$-CeO_2/NF, it was utilized as an anode and a cathode for assembling a water electrolyzer ($NiFe_2O_4$-$Fe_{24}N_{10}$-CeO_2/NF||$NiFe_2O_4$-$Fe_{24}N_{10}$-CeO_2/NF). The $NiFe_2O_4$-$Fe_{24}N_{10}$-CeO_2/NF also displays good performance with a potential of 1.81 V at 100 mA·cm^{-2} for OWS, which is superb to $NiFe_2O_4$-$Fe_{24}N_{10}$/NF (1.83 V), CeO_2/NF (1.96 V), precursor (1.89 V) and NF (1.90 V). The OWS stability test of $NiFe_2O_4$-$Fe_{24}N_{10}$-CeO_2/NF demonstrates that it can continuously operate for 30 h at 500 mA·cm^{-2} with voltage rise of only 0.2 V (Fig. 6b), indicating its potential for industrial application.

4. Conclusions

In summary, the CeO_2 electronic structure modulated FeNi bimetallic composite porous nanosheets *in-situ* grown on 3D NF are prepared through a solvothermal and annealing method. Benefiting from the electronic interaction of CeO_2 modulating the electronic structure of FeNi composite and self-supporting porous nanosheets, the prepared $NiFe_2O_4$-$Fe_{24}N_{10}$-CeO_2/NF exhibited excellent water electrolysis activity with a low potential of 1.81 V to arrive at 100 mA·cm^{-2} for OWS. It also displays good stability at 500 mA·cm^{-2} for 30 h with no significant potential augment. These results indicate that the $NiFe_2O_4$-$Fe_{24}N_{10}$-CeO_2/NF meets the requirements of high efficiency and prolonged stable operation at large current

density. Hence, this work has implications for designing bifunctional catalysts applied in industrial water electrolysis hydrogen production.

Acknowledgements

This work is supported by the National Natural Science Foundation of China (22162004), and the Natural Science Foundation of Guangxi Province (2022JJD120011).

References

[1] Lu H S, He X B, Yin F X, Li G R. Preparations of nickel-iron hydroxide/sulfide and their electrocatalytic performances for overall water splitting[J]. J. Electrochem., 2020, 26(1): 136−147.

[2] Song M, Zhao Y, Wu Z X, Liu X E. MoS_2/CoB with Se doping on carbon cloth to drive overall water-splitting in an alkaline electrolyte[J]. Sustain. Energ. Fuels, 2020, 4(10): 5036−5041.

[3] Ma D D, Shi J W, Sun L W, Sun Y X, Mao S M, Pu Z X, He C, Zhang Y J, He D, Wang H K, Cheng Y H. Knack behind the high performance CdS/ZnS-NiS nanocomposites: optimizing synergistic effect between cocatalyst and heterostructure for boosting hydrogen evolution[J]. Chem. Eng. J., 2022, 431: 133446.

[4] Li Y, Luo Z Y, Ge J J, Liu C P, Xing W. Research progress in hydrogen evolution low noble/non-precious metal catalysts of water electrolysis[J]. J. Electrochem., 2018, 24(6): 572−588.

[5] Chen S S, Hisatomi T, Ma G J, Wang Z, Pan Z H, Takata T, Domen K. Metal selenides for photocatalytic Z-scheme pure water splitting mediated by reduced graphene oxide [J]. Chin. J. Catal., 2019, 40(11): 1668−1672.

[6] Niu S, Jiang W J, Tang T, Yuan L P, Luo H, Hu J S. Autogenous growth of hierarchical NiFe(OH)$_x$/FeS nanosheet-on-microsheet arrays for synergistically enhanced high-output water oxidation[J]. Adv. Funct. Mater., 2019, 29(36): 1902180.

[7] Shi Y M, Yu Y, Liang Y, Du Y H, Zhang B. *In situ* electrochemical conversion of an ultrathin tannin nickel iron complex film as an efficient oxygen evolution reaction electrocatalyst[J]. Angew. Chem. Int. Ed., 2019, 58(12): 3769−3773.

[8] Yu L, Yang J F, Guan B Y, Lu Y, Lou X W. Hierarchical hollow nanoprisms based on ultrathin Ni-Fe layered double hydroxide nanosheets with enhanced electrocatalytic activity towards oxygen evolution[J]. Angew. Chem., Int. Ed., 2018, 57(1): 172−176.

[9] Cui X J, Ren P J, Deng D H, Deng J, Bao X H. Single layer graphene encapsulating non-precious metals as high-performance electrocatalysts for water oxidation[J]. Energy Environ. Sci., 2016, 9(1): 123−129.

[10] Tao J Y, Zhang Y J, Wang S P, Wang G, Hu F, Yan X J, Hao L F, Zuo Z J, Yang X W. Activating three-dimensional networks of Fe@Ni nanofibers via fast surface modification for efficient overall water splitting[J]. ACS Appl. Mater. Inter., 2019, 11(20): 18342−18348.

[11] Ma E H, Liu X P, Shen T, Wang D L. Constructing carbon-encapsulated NiFeV-based electrocatalysts by alkoxide-based self-template method for oxygen evolution reaction [J]. J. Electrochem., DOI: 10.13208/j.electrochem.211103.

[12] Zou Y J, Xiao B, Shi J W, Hao H, Ma D D, Lv Y X, Sun G T, Li J, Cheng Y H. 3D hierarchical heterostructure assembled by NiFe LDH/(NiFe)S_x on biomass-derived hollow carbon microtubes as bifunctional electrocatalysts for overall water splitting[J]. Electrochim. Acta, 2020, 348: 136339.

[13] Wang M, Zhang L, Pan J L, Huang M R, Zhu H W. A highly efficient Fe-doped Ni_3S_2 electrocatalyst for overall water splitting[J]. Nano Res., 2021, 14(12): 4740−4747.

[14] Friebel D, Louie M W, Bajdich M, Sanwald K E, Cai Y, Wise A M, Cheng M J, Sokaras D, Weng T C, Alonso M R, Davis R C, Bargar J R, Norskov J K, Nilsson A, Bell A T. Identification of highly active Fe sites in (Ni, Fe)OOH for electrocatalytic water splitting[J]. J. Am. Chem. Soc., 2015, 137(3): 1305−1313.

[15] Subbaraman R, Tripkovic D, Chang K C, Strmcnik D, Paulikas A P, Hirunsit P, Chan M, Greeley J, Stamenkovic V, Markovic N M. Trends in activity for the water electrolyser reactions on 3d M (Ni, Co, Fe, Mn) hydr(oxy)oxide catalysts[J]. Nat. Mater., 2012, 11(6): 550−557.

[16] Shah J H, Xie Q X, Kuang Z C, Ge R L, Zhou W H, Liu D R, Rykov A I, Li X N, Luo J S, Wang J H. *In-situ/operando* ^{57}Fe Mössbauer spectroscopic technique and its applications in NiFe-based electrocatalysts for oxygen evolution reaction [J]. J. Electrochem., 2022, 28(3): 2108541.

[17] Chen H Y, Hu M H, Jing P, Liu B C, Gao R, Zhang J. Constructing heterostructure of CeO_2/WS_2 to enhance catalytic activity and stability toward hydrogen generation [J]. J. Power Sources, 2022, 521: 230948.

[18] Zheng Z, Li N, Wang C Q, Li D Y, Zhu Y M, Wu G. Ni-CeO_2 composite cathode material for hydrogen evolution reaction in alkaline electrolyte[J]. Int. J. Hydrogen Energy, 2012, 37(19): 13921−13932.

[19] Lu M J, Chen D, Wang B, Li R Q, Cai D, Tu H R, Yang H, Zhang Y P, Han W. Boosting alkaline hydrogen evolution performance of Co_4N porous nanowires by interface engineering of CeO_2 tuning[J]. J. Mater. Chem. A, 2021, 9(3): 1655−1662.

[20] Zhang R, Ren X, Hao S, Ge R X, Liu Z A, Asiri A M, Chen L, Zhang Q J, Sun X P. Selective phosphidation: an effective strategy toward CoP/CeO_2 interface engineering for superior alkaline hydrogen evolution electrocatalysis[J]. J. Mater. Chem. A, 2018, 6(5): 1985−1990.

[21] Chen Z H, Ma Z P, Song J J, Wang L X, Shao G J. A novel approach for the preparation of Ni-CeO_2 composite cathodes with enhanced electrocatalytic activity[J]. RSC Adv., 2016, 6(65): 60806−60814.

[22] Sivanantham A, Ganesan P, Shanmugam S. A synergistic effect of Co and CeO_2 in nitrogen-doped carbon nanostructure for the enhanced oxygen electrode activity and stability[J]. Appl. Catal., B, 2018, 237: 1148−1159.

[23] Gao W, Wen D, Ho J C, Qu Y. Incorporation of rare earth elements with transition metal-based materials for electrocatalysis: a review for recent progress[J]. Mater. Today Chem., 2019, 12: 266−281.

[24] Feng J X, Ye S H, Xu H, Tong Y X, Li G R. Design and synthesis of FeOOH/CeO_2 heterolayered nanotube electrocatalysts for the oxygen evolution reaction[J]. Adv. Mater., 2016, 28(23): 4698−4703.

[25] Zhou H Q, Yu F, Zhu Q, Sun J Y, Qin F, Yu L, Bao J M, Yu Y, Chen S, Ren Z F. Water splitting by electrolysis at high current densities under 1.6 volts[J]. Energy Environ. Sci., 2018, 11(10): 2858−2864.

[26] Yu X T, Wang M Y, Gong X Z, Guo Z C, Wang Z, Jiao S Q. Self-supporting porous CoP-based films with phase-separation structure for ultrastable overall water electrolysis at large current density[J]. Adv. Energy Mater., 2018, 8(34): 1802445.

[27] Mao L Q, Ba Q Q, Jia X J, Liu S, Liu H, Zhang J, Li X J, Chen W. Ultrathin Ni(OH)$_2$ nanosheets: a new strategy for cocatalyst design on CdS surfaces for photocatalytic hydrogen generation[J]. RSC Adv., 2019, 9(3): 1260−1269.

[28] Li G L, Zhang X B, Zhang H. Ultrathin 2D Nanosheet based 3D hierarchical hollow polyhedral CoM/C (M = Ni, Cu, Mn)

phosphide nanocages as superior electrocatalysts toward oxygen evolution reaction[J]. Chem. Eng. J., 2020, 398: 125467.
[29] Wang J Y, Zhu R L, Cheng J L, Song Y Y, Mao M, Chen F F, Cheng Y L. Co, Mo_2C encapsulated in N-doped carbon nanofiber as self-supported electrocatalyst for hydrogen evolution reaction[J]. Chem. Eng. J., 2020, 397: 125481.
[30] Yu T Q, Xu Q L, Luo L, Liu C R, Yin S B. Interface engineering of NiO/RuO_2 heterojunction nano-sheets for robust overall water splitting at large current density[J]. Chem. Eng. J., 2022, 430: 133117.
[31] Ji R Y, Chan D S, Jow J J, Wu M S. Formation of open-ended nickel hydroxide nanotubes on three-dimensional nickel framework for enhanced urea electrolysis[J]. Electrochem. Commun., 2013, 29: 21−24.
[32] Wang Y M, Qian G F, Xu Q L, Zhang H, Shen F, Luo L, Yin S B. Industrially promising IrNi-$FeNi_3$ hybrid nanosheets for overall water splitting catalysis at large current density[J]. Appl. Catal., B, 2021, 286: 119881.
[33] Sun Z H, Cao X C, Gonzalez M IG, Rümmeli M H, Yang R Z. Enhanced electrocatalytic activity of $FeCo_2O_4$ interfacing with CeO_2 for oxygen reduction and evolution reactions[J]. Electrochem. Commun., 2018, 93: 35−38.
[34] Trotochaud L, Young S L, Ranney J K, Boettcher S W. Nickel-iron oxyhydroxide oxygen-evolution electrocatalysts: the role of intentional and incidental iron incorporation[J]. J. Am. Chem. Soc., 2014, 136(18): 6744−6753.
[35] Feng Z H, Pu J Y, Liu M S, Zhang W X, Zhang X Y, Cui L, Liu J Q. Facile construction of hierarchical Co_3S_4/CeO_2 heterogeneous nanorod array on cobalt foam for electrocatalytic overall water splitting[J]. J. Colloid Interface Sci., 2022, 613: 806−813.
[36] Chen L L, Jang H, Kim M G, Qin Q, Liu X, Cho J. Fe_xNi_y/CeO_2 loaded on N-doped nanocarbon as an advanced bifunctional electrocatalyst for the overall water splitting[J]. Inorg. Chem. Front., 2020, 7(2): 470−476.
[37] Park K R, Tran D T, Nguyen T T, Kim N H, Lee J H. Copper-incorporated heterostructures of amorphous $NiSe_x$/Crystalline $NiSe_2$ as an efficient electrocatalyst for overall water splitting[J]. Chem. Eng. J., 2021, 422: 130048.
[38] Zhang J, Wang T, Rellinghaus D PB, Dong R H, Liu S H, Zhuang X D, Feng X L. Interface engineering of MoS_2/Ni_3S_2 heterostructures for highly enhanced electrochemical overall-water-splitting activity[J]. Angew. Chem., Int. Ed., 2016, 55(23): 6702−6707.
[39] Qian G F, Chen J L, Luo L, Zhang H, Chen W, Gao Z J, Yin S B, Tsiakaras P. Novel bifunctional V_2O_3 nanosheets coupled with N-doped-carbon encapsulated Ni heterostructure for enhanced electrocatalytic oxidation of urea-rich wastewater[J]. ACS Appl. Mater. Inter., 2020, 12(34): 38061−38069.
[40] Wu M X, Zhang G X, Qiao J L, Chen N, Chen W F, Sun S H. Ultra-long life rechargeable zinc-air battery based on high-performance trimetallic nitride and NCNT hybrid bifunctional electrocatalysts[J]. Nano Energy, 2019, 61: 86−95.
[41] Watkins M B, Foster A S, Shluger A L. Hydrogen cycle on CeO_2(111) surfaces: density functional theory calculations [J]. J. Phys. Chem. C, 2007, 111(42): 15337−15341.

CeO_2 电子调控 FeNi 纳米片大电流密度电解水催化剂

丁明宇，蒋文杰，余天琦，卓小燕，覃晓静，尹诗斌*
广西电化学能源材料重点实验室，广西大学化学化工学院，广西 南宁 530004

摘要

开发高活性的大电流密度非贵金属双功能催化剂对于电解水制氢的发展意义重大。本文通过水热法和高温退火处理制备了自生长在泡沫镍上的 CeO_2 电子调控的 FeNi 双金属复合物多孔纳米片（$NiFe_2O_4$-$Fe_{24}N_{10}$-CeO_2/NF）。电化学测试结果表明，$NiFe_2O_4$-$Fe_{24}N_{10}$-CeO_2/NF 在 1.0 mol·L^{-1} KOH 电解液中具有出色的析氧和析氢反应（OER 和 HER）活性，在±1000 mA·cm^{-2} 电流密度下所需的过电位分别为 352 mV 和 429 mV。将其组装成电解水（OWS）两电极体系，只需 1.81 V 的电池电压就能达到 100 mA·cm^{-2} 的电流密度。对于 OER、HER 和 OWS，可以在±500 mA·cm^{-2} 的电流密度下稳定运行 30 小时，其优异的大电流密度催化性能可以归功于 CeO_2 对于 FeNi 复合物的电子结构调控增强了催化剂的本征活性和反应中间体的吸附。原位生长在泡沫镍（NF）上的多孔纳米片可以增强活性位点与电解质的接触，并利于气体产物的释放，从而提高其化学稳定性和机械稳定性。本工作为制备双功能非贵金属电解水催化剂提供了一种新思路。

关键词：FeNi 复合物；析氢反应；析氧反应；催化剂；电解水